LJMU Research Online

Grubben, TM, Baker, JL, Parez, S and Einav, I

 Role of inertia in the starting and stopping mechanisms of granular flows

http://researchonline.ljmu.ac.uk/id/eprint/25775/

Article

For more information please contact researchonline@ljmu.ac.uk

The role of inertia in the starting and stopping mechanisms of granular flows

T.M. Grubben

Faculty of Civil Engineering and Geosciences,

Delft University of Technology, The Netherlands

J.L. Baker

School of Computer Science and Mathematics,

Liverpool John Moores University, United Kingdom

S. Parez

Institute of Chemical Process Fundamentals,

Czech Academy of Sciences, Czech Republic and

Faculty of Science, Jan Evangelista Purkyně University

in Ústí nad Labem, Czech Republic

I. Einav[*]

School of Civil Engineering, The University of Sydney, Australia

(Dated: March 4, 2025)

Abstract

It is well-known that a pile of grains starts and stops flowing at different angles of repose. It is also known that such starting and stopping angles exhibit thickness-dependent behaviour, with deeper layers beginning to flow more readily and arresting at lower angles than shallower materials. These considerations have motivated various rheological assumptions in granular constitutive laws. This paper demonstrates that such observations can instead be partly attributed to inertial effects. In particular, we examine the roles of two control parameters characterising conventional chute flow experiments: the rate of inclination of the chute, and the threshold surface velocity associated with identification of the flow. Both of these parameters control the system's momentum at different instances. We perform two-dimensional discrete-element simulations and also develop a one-dimensional analytic model based on the standard $\mu(I)$-rheology. Results indeed indicate a difference between the starting and stopping angles as well as a thickness-dependency, despite the absence of any hysteresis or material length scale in the underlying rheological model. Higher threshold velocities are shown to produce higher angles at which flow begins. In addition, the starting/stopping angle increases/decreases with the applied inclination rate. For thick enough granular layers, no matter how small the rate is, critical angles are shown to deviate from the quasi-static limit. Therefore, inertial effects should not *a priori* be neglected. To finalise our argument, we show the effect of the inclination rate and the threshold velocity in a laboratory set-up, using small-scale experiments of an inclined chute.

I. INTRODUCTION

For many years, the focus of granular media research has been on the development of appropriate constitutive laws describing complex flow phenomena. While there has been much progress on this front that has sustained and stimulated the field, the question of one all-encompassing rheological model remains open for debate, especially at the transition between flowing and stationary regimes. Without further contributing to the discussion by exploring new constitutive assumptions, this paper wishes to explore slightly different questions: how do inertial effects influence the starting and stopping mechanisms of granular

---

* itai.einav@sydney.edu.au

systems? Can these effects alone explain the complex flow phenomena previously observed? The findings could have immediate implications for modelling the dynamics of shearing granular media, such as landslides, avalanches and earthquake faults (*e.g.* [1, 2]).

Even though no overall consensus has been reached yet, one of the most widely accepted constitutive laws for granular materials is the local $\mu(I)$-rheology, where the effective friction coefficient μ depends on the inertial number I, a non-dimensional parameter accounting for the stress, shear rate, particle diameter, particle density and packing fraction [3–5]. This theory has successfully been applied to a wide range of granular flow configurations in the intermediate (fluid-like) regime, owing its popularity to its applicability and relative simplicity [6]. Despite being initially constructed for steady flows, the $\mu(I)$-rheology has proven surprisingly effective even for unsteady flow regimes (*e.g.* [7, 8]) and, in adapted form, for complex granular flows [9]. However, in some transient cases, the predictions of this local law do appear to deviate from experimental results, in particular near the flow to no-flow transition.

One common discrepancy is with inclined-plane experiments [e.g. 10], which typically involve beginning with a stationary layer of material on a shallow incline. The inclination angle is then gradually increased until the static material begins to flow, at which point the elevation is fixed, defining the starting flow angle for a given layer thickness. If the experiment is conducted with a thicker layer of material, the flow is initiated more readily at a lower inclination angle. Similarly, once flow has begun, the material erodes downward before coming to a halt, leaving behind a shallower stationary layer of material at the same inclination angle. On the other hand, the inclination angle of a flowing sample can be reduced below the starting angle of repose until the motion ceases, determining the stopping flow angle, again for a given thickness [e.g. 11]. While these experimental observations have been used to inspire and inform the granular $\mu(I)$-rheology, the model typically struggles to reproduce the full hysteretic behaviour without introducing additional rheological constraints.

Without presenting new rheological parameters, the aim of this study is to take a step back and shed light on the role of the inertia (as per its classical definition in physics) of the granular mass. It will examine to what extent inertia can explain the experimental observations around the flow to no-flow transition of granular material by examining the effect of two protocol parameters. These protocol parameters are the rate of inclination and threshold velocity. The latter parameter represents the inevitable experimental velocity at

which the grains are considered to start moving. In rotating chute experiments (*e.g.* [10]) an observer — whether human or programmed machinery — needs a non-zero criterion to detect motion. Further acceleration of the grains exist during the human/programmed machinery's reaction time to this event, and during the time taken by the experimental machinery to then act in response. The threshold u_t provides a value that agglomerates these three unavoidable experimental factors. In a similar fashion to the thickness of the layer, both the rate of inclination and threshold velocity are expected to contribute to the generation of momentum, thereby affecting the starting and stopping angle. Therefore, we hypothesise that, provided inertia effects are taken into account, the difference between the critical starting and stopping angle and their dependence on thickness can be replicated by a continuum model in its simplest form: a one-dimensional momentum balance equation of the standard incompressible $\mu(I)$-rheology.

In order to be able to isolate the inertia effects, we firstly perform Discrete Element Method (DEM) analysis. This allows us to represent and study the boundary value problem in a controlled manner that eliminates erosion mechanisms at the inlet and outlet of the flow by considering a periodic two-dimensional shear layer, mimicking an infinitely long slope. Subsequently, we present a one-dimensional, depth-resolved continuum solution of the $\mu(I)$-rheology that corresponds to the configuration used in the DEM simulations. The ability of this solution to describe the starting and stopping thresholds of granular flows is evaluated in order to analytically assess the role of inertia in transient granular flows. Finally, we perform inclined chute experiments to verify our findings in a non-idealised set-up.

II. INCLINED CHUTE WITHOUT EROSION: DEM AND CONTINUUM MODELS

Conventional chute flow experiments use a setup in which the inclination angle is gradually changed until flow is initiated or ceased (*e.g.* [10]). The onset of the flow is determined by an observer when they consider the grains to have reached a sufficient velocity. As a result, the rate of inclination and the threshold velocity of the flow surface are two parameters which control the amount of momentum in the system and affect the measurement of the flow transition. However, these are rarely accurately reported. To investigate the effect of these parameters in a controlled manner, we first adopt a simplified modelling setup: a
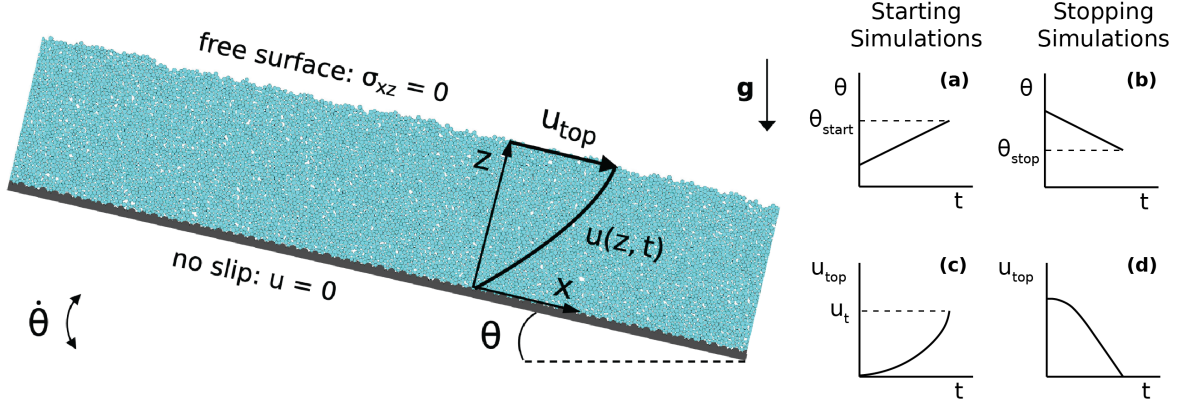
FIG. 1. Numerical simulation setup. A granular layer is placed on a rough slope whose inclination angle θ is changed at a constant rate $\dot{\theta}$. The flow is considered homogeneous in the downslope direction x, like on an infinite slope, and thus depends only on the normal coordinate z. The surface velocity u_{top} is monitored to identify onset or cessation of the flow and the associated critical angle. On the right-hand side, the panels (a)-(d) present the development of θ and u_{top} over time for both the starting and the stopping simulations.

one-dimensional, mass-conserving flow down an infinite chute. Such a setup represents a boundary value problem, which is solved here by means of both DEM simulations and an analytic continuum model.

For both the DEM and the continuum approaches, the following protocol, illustrated in Figure 1, is imposed to determine the angles of repose for flow onset and cessation. In the case of flow initiation, a granular layer of thickness h is at rest on a mild slope, $\theta_0 = 8°$, well below the static angle of repose. Next, the inclination angle of the slope, θ, is increased at a given constant rate $\dot{\theta} > 0$. This continues until the velocity at the top surface of the flow (averaged over all downslope positions x) reaches a specified threshold velocity, $u_{top} = u_t$, see Figure 1c. The corresponding inclination angle at this time, θ_{start}, represents the static angle of repose, see Figure 1a. For the simulation of flow cessation, the same granular layer with static thickness h is initially flowing down a slope of $\theta_0 = 24°$, well above the static angle of repose, at a steady-state velocity. Subsequently, the inclination angle is decreased at a prescribed rate $\dot{\theta} < 0$ until the flow comes to a rest, $u_{top} = 0$, see Figure 1d. The corresponding inclination angle at this time, θ_{stop} (see Figure 1b) represents the dynamic angle of repose.

A. Discrete Element Model

The DEM represents grains as spheres interacting via elasto-frictional contact forces [12]. Motion of individual grains is evolved according to Newton's laws for the translational and rotational degrees of freedom. Full details on the method can be found in Appendix A and in previous works [13, 14], but a summary of the key information is given below.

We adopt the spring-dashpot contact law to describe pair-wise contact forces between grains. Normal and tangential forces acting on particle i due to particle j are

$$\mathbf{F}_{ij}^n = -k_n \delta_{ij} \mathbf{n}_{ij} + \gamma_n m_{\text{eff}} \mathbf{u}_{ij}^n \,,$$

$$\mathbf{F}_{ij}^t = k_t \mathbf{t}_{ij} + \gamma_t m_{\text{eff}} \mathbf{u}_{ij}^t \,, \qquad \text{if} \quad F_{ij}^t < \mu_g F_{ij}^n \,,$$

$$\mathbf{F}_{ij}^t = \mu_g F_{ij}^n \frac{\mathbf{t}_{ij}}{t_{ij}} \,, \qquad\qquad \text{otherwise} \,,$$

where k_n and k_t are normal and shear stiffnesses of the contact, characterised by normal deflection δ_{ij} and tangential displacement $\mathbf{t}_{ij}$ (see Appendix A for their definitions); $\mathbf{n}_{ij}$ denotes a unit vector normal to the contact plane and pointing from i to j; γ_n and γ_t are damping coefficients, m_{eff} is the effective mass of particles i and j, and $\mathbf{u}_{ij}^n$ and $\mathbf{u}_{ij}^t$ are relative velocities of the two particles projected into the normal and the tangential directions. The tangential component of the inter-particle force is truncated by the Coulomb limit $\mu^* F_{ij}^n$, where μ^* is grain surface friction coefficient.

The DEM parameters used in this work are listed in Table I. Grain density and size match the values used in the experiment. Young's modulus of a grain, $E = k_n/d = 7 \cdot 10^8$ Pa, is about two orders of magnitude lower than a realistic value in order to speed up the simulations. In particular, while it is critical to resolve fast grain collisions in the DEM, flow of grains arises from their rearrangements, which occur on a much longer time scale. The time scale of grain collisions $t_{\text{col}} = d\sqrt{\rho/E}$ is artificially increased by reducing E so that less time steps are needed to propagate the system between macroscopic grain rearrangements. Previous studies have shown that under low stresses (as is the situation here), granular dynamics is insensitive to the value of the elastic modulus [13, 15]. The damping coefficient γ_n corresponds to the normal coefficient of restitution of 0.57. The relatively low restitution coefficient was chosen to quickly dampen vibrations of grains to minimise their contributions to surface velocity u_{top}, which is monitored to determine the start/stop of the flow. The restitution coefficient has been shown to have little effect on the flow behaviour except for

TABLE I. Parameters of DEM simulations

Parameter	Symbol	Value
grain density	ρ	2500 kg m^{-3}
mean grain size	d	0.75 mm
polydispersity		$\pm 20\%$
normal stiffness coefficient	k_n	$5.2 \cdot 10^5 \text{ Pa m}$
tangential stiffness coefficient	k_t	$2.6 \cdot 10^5 \text{ Pa m}$
normal damping coefficient	γ_n	$4.9 \cdot 10^5 \text{ s}^{-1}$
tangential damping coefficient	γ_t	0 s^{-1}
grain surface friction coefficient	μ^*	0.5

the high-inertia collisional regime [15, 16]. The dominant mechanism for energy dissipation in dense granular flows arises from the friction force $F_{ij}^t = \mu^* F_{ij}^n$ [15]. On that basis, we neglect the damping in the tangential force by setting $\gamma_t = 0$.

Granular layers are initialised as random packings by pouring grains onto a flat surface. The slope is then increased to $24°$ to establish steady flow. For the simulations of flow onset, the slope is subsequently lowered to $8°$ to produce the initial static configuration. Along with Figure 1, periodic boundary conditions are applied in the x (downslope) direction to simulate a mass-conserving flow. This is equivalent to flow down an infinitely long chute. The size of the periodic cell is $L_x = 200d$, where d is the mean diameter of the particles, which are slightly (20%) polydisperse. For a single layer thickness $h = 70d$, the simulations were repeated using $L_x = 96d$ to check that the finite size effects are small.

For the sake of reducing computational time and simplifying the analysis, while preserving the main features of the model, three-dimensional grains form a monolayer in the xz plane. Their motion is thus restricted to x (downslope) and z (perpendicular to the slope) directions, making the system dynamics two-dimensional. Moreover, due to the periodic boundaries, flow is roughly homogeneous along the x direction and its properties vary in z only. The slope is rough, made of glued grains with alternating sizes $0.5d$ ($\pm 20\%$) and $2.5d$ ($\pm 20\%$). The alternating size of the rough granular bottom induces efficient interlocking of grains along the bottom of the flow, providing a no-slip boundary condition.

B. Depth-Resolved Continuum Model

Presented here is the continuum solution as a first-order approximation to the one-dimensional boundary-value problem corresponding to the setup from Figure 1. For the derivation, we follow a previous approach [8, 17] and adopt linearised incompressible $\mu(I)$-rheology [5]. Considering a chute plane aligned at an angle θ to the horizontal, with x representing the downslope direction and z the direction normal to the base, we impose a no-slip boundary condition at the chute plane ($z = 0$) and stress-free boundary conditions at the free surface of the flow ($z = h$). Assuming a system that is invariant by rotation and translation, the reduced components of the momentum balance equation are then given by

$$\rho\phi\frac{\partial u}{\partial t} = \frac{\partial \sigma_{xz}}{\partial z} + \rho\phi g \sin\theta, \tag{1}$$

$$\rho\phi\frac{\partial w}{\partial t} = \frac{\partial \sigma_{zz}}{\partial z} + \rho\phi g \cos\theta. \tag{2}$$

Here, u is the downslope (x) velocity, w the velocity in the z-direction normal to the base, t the time, θ the time-dependent inclination angle, σ_{xz} the shear stress, σ_{zz} the normal stress, ρ the intrinsic solid density of the grains, ϕ the solid fraction, and g the gravitational acceleration. Given our assumption of a system invariant by translation and $w = 0$ at the base of the flow, the flow velocity in the direction normal to the base is identically zero, therefore, equation (2) can be integrated to solve for the normal stress

$$\sigma_{zz} = \rho\phi g \cos\theta(h - z), \tag{3}$$

which vanishes at the top of the layer. Closing off the system of equations, the solution solely utilises the momentum equation of the standard incompressible $\mu(I)$-rheology and does not require any additional constitutive assumptions. In this one-dimensional flow regime, this constitutive law in linearised form simplifies to

$$\sigma_{xz} = \mu(I)\sigma_{zz}\,\mathrm{sgn}\left(\frac{\partial u}{\partial z}\right) \quad \text{and} \quad \mu(I) = \mu_s + \beta I, \tag{4}$$

where sgn is the sign function, and μ_s and β are material-dependent rheological parameters [3, 5]. The inertial number I is a non-dimensional variable representing the ratio of the macroscopic timescale for bulk deformation to the microscopic timescale for grain rearrangements. For flow that depends only on the normal direction z, the inertial number simplifies

TABLE II. Rheological parameters used in the continuum model differentiating between the imposed parameters and parameters inferred from the DEM analysis.

Parameter	Symbol	Value
Imposed		
grain density	ρ	2500 kg m^{-3}
mean grain size	d	0.75 mm
Inferred from DEM		
solid fraction	ϕ	0.52
static friction coefficient	μ_s	0.274
rheological material parameter	β	0.93

to

$$I = \left| \frac{\partial u}{\partial z} \right| d \sqrt{\frac{\rho}{\sigma_{zz}}}, \tag{5}$$

where d is the particle diameter. This complete system of equations (1)-(5) is solved for the downslope velocity $u(z,t)$ using a custom RK4 finite difference scheme in MATLAB. To allow comparison between different rates while minimising the numerical error, the simulation time step is rate-dependent $\Delta t = 1e^{-7}\dot{\theta}^{-1}$.

Table II lists the parameters that have been used in the continuum model. They are chosen to match the DEM simulations. The solid fraction varies between $0.5 - 0.6$ in the DEM simulations, as granular layers dilate during flow. In the continuum model, this variation is neglected, and a single value $\phi = 0.52$ is selected along with the assumption of incompressible flow. The $\mu(I)$ parametrization, given by μ_s and β, is consistent with the rheology observed in DEM simulations; the selected values reproduce well the steady-state velocity as well as the shear stress to normal stress ratio. It should be noted that the values of rheological parameters inferred from DEM are influenced by the dimension of the DEM model (2D vs 3D). Nevertheless, the difference between the rheological parameters used here and the experimental values for glass beads inferred in other studies [5, 10, 18, 19] is within a factor of two.

C. Quasi-Static Variation of the Inclination Angle

In the setup under consideration, the inclination angle θ varies with time. However, if this variation is slow enough, the flow velocity approaches the same velocity that would be achieved for a fixed slope inclined at the current angle θ. Such "quasi-static" velocity depends on the current value of θ and not on the rate of inclination $\dot{\theta}$ and can be formulated analytically by neglecting the inertia term in the momentum conservation equation (1). As a result, the shear stress increases linearly with the depth in the layer, similarly to the normal stress, such that their ratio $\mu = \tan \theta$. This value of μ corresponds to a unique value of I, from which the steady-state shear rate can be derived, and consequently, integrated to find the steady-state velocity profile obeying Bagnold's form [3, 8]:

$$u(z) = \int_0^z \frac{\partial u(z')}{\partial z'}\, dz' = \frac{2(\tan \theta - \mu_s)\sqrt{\phi g \cos \theta}}{3\beta d}\left[h^{3/2} - (h-z)^{3/2}\right]. \tag{6}$$

By definition, θ_{start} is the angle at which the flow velocity reaches the threshold velocity u_t at the top surface ($z = h$). For that reason, in this quasi-static regime in terms of inclination angle variation, we can substitute into (6) and rearrange to see that h, u_t and θ_{start} satisfy the equation

$$h = \left[\frac{3\beta d u_t}{2(\tan \theta_{start} - \mu_s)\sqrt{\phi g \cos \theta_{start}}}\right]^{2/3}. \tag{7}$$

Similarly, θ_{stop} complies with (6) when $u_t = 0$, and thus $\tan \theta_{stop} = \mu_s$. For the value of the static friction coefficient used here (see Table II), this produces a value $\theta_{stop} = 15.3°$.

D. Results

We evaluate the potential of the continuum solution to describe the flow to no-flow transition by comparing the results with the DEM solution. Both solutions follow the same numerical protocol as illustrated in Figure 1. Furthermore, a comparison between the continuum solution and the quasi-static solution allows us to examine the effect of inertia.

1. Development of the Flow

We begin the analysis by interpreting how the flow evolves for different inclination rates, considering $|\dot{\theta}| = 0.1$, 1 and 10 °/s. Here, the inclination angle is thus perpetually increasing/decreasing with time and no velocity threshold is imposed. The results are summarised

10

in Figure 2, where the top Figures 2a - c and bottom Figures 2d - f depict the results for the starting and stopping simulations, respectively. The static thickness of the layer is $h = 110d$ in all cases. The agreement between the continuum and DEM solution is good, albeit with some small discrepancies appearing between the two solutions. This could be explained by the fact that the solid fraction ϕ is not constant for the DEM solution, but which is assumed constant $\phi = 0.52$ for the continuum solution. This ingredient could easily be added to the continuum model by considering a dependence of the solid fraction on the inertial number, as shown by previous studies [5, 15].

Figures 2a and d illustrate the velocity profile with respect to the depth z of the granular layer when $\theta = 20°$. For the starting simulations, it can be observed that the flow is more developed for the slow rate. On the other hand, the results of the stopping simulations show a velocity profile which is closer to rest for the slow rate. Both these observations illustrate the relevance of the rate of inclination $\dot{\theta}$ with respect to the transient time needed for the flow to adjust to a new steady-state. The lower the rate of inclination, the closer the velocity is to the quasi-static solution given by (6).

A similar interpretation can be made from Figures 2b and e, showing the evolution of the velocity at the top of the layer u_{top} with the inclination angle θ. Again, the results for the slowest rate tightly follow the quasi-static solution. By increasing the rate of inclination, the results deviate from the quasi-static solution, showing a generally lower trend of u_{top} with respect to θ. Consequently, in the stopping simulations, the fastest rate even predicts a moving granular layer for negative (upslope) inclination angles. Finally, in Figures 2c and f, the development of u_{top} has been plotted over time. For the starting simulations shown in Figure 2c, $t = 0$ corresponds to the time that $\theta = \arctan \mu_s$, while for Figure 2f, $t = 0$ represents the initial steady state conditions. Both the DEM and continuum solutions predict a higher acceleration (starting simulations) or deceleration (stopping simulations) of the flow with increasing rate.

In summary, faster rates of inclination lead to greater inertia of the flow. This is demonstrated by the greater magnitude of acceleration $|\partial u/\partial t|$. However, the change of flow velocity with θ, that is $\partial u/\partial\theta = (\partial u/\partial t)/\dot{\theta}$, becomes lower for higher rates of inclination. The maximum $\partial u/\partial\theta$ is achieved for vanishing rate of inclination. This limit corresponds to the quasi-static solution characterised by negligible inertia, when the flow velocity is the steady-state velocity (6) at the actual inclination θ. With increasing the rate of inclination,
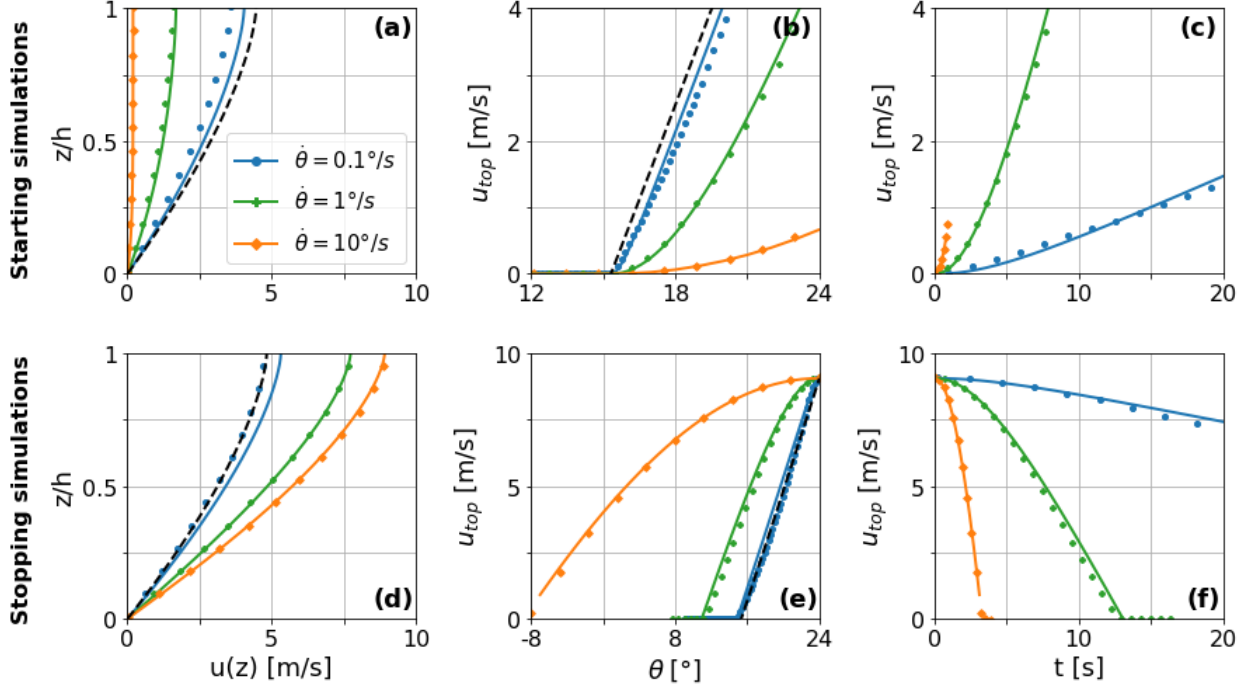
FIG. 2. Development of the flow according to the DEM solution (markers), continuum solution (solid lines) and quasi-static solution (6) (black, dashed line) for a continuously increasing/decreasing inclination angle θ. Firstly, velocity profiles are shown at a point in time when $\theta = 20°$ for the a) starting and d) stopping simulations. Secondly, the evolution of the surface velocity u_{top} is shown as a function of θ for the b) starting and e) stopping simulations. Thirdly, the evolution of the surface velocity u_{top} is shown as a function of time t for the c) starting and f) stopping simulations.

inertial effects become significant, as the flow does not have enough time to adjust to the changing inclination. The analysis of corresponding time scales will be elaborated on at the end of this section.

2. Assessment of the Inertia Effects

In the next analysis, we perform the starting and stopping simulations for various static thicknesses of the granular layer h and the three rates of inclination. For the starting simulations, we consider a velocity threshold $u_t = 0.1$ m/s. This value is chosen because it aligns well with the measured values in our experiments (see Section III B). In terms of

the stopping simulations, for simplicity, we use $u_t = 0$ m/s for the continuum solution. In the DEM model, the velocity of the particles remains finite due to small vibrations of the particles, and thus the cessation of the flow is established at $u_t = 7 \cdot 10^{-4}$ m/s.

The results are shown in Figure 3. The key findings are: Firstly, and in line with the expectations, a higher inclination rate increases θ_{start} and decreases θ_{stop}, and thus greater apparent hysteresis $\Delta\theta = \theta_{start} - \theta_{stop}$. This is consistent with the slower evolution of flow velocity with θ observed in Figures 2b and e, where an arbitrary threshold velocity $u_{top} = u_t$ is reached for higher θ_{start} and lower θ_{stop} at greater inclination rate (*e.g.* orange vs blue lines). Interestingly, in Figure 3c, the minima of the apparent hysteresis seem to closely follow the critical thickness h_c for the different inclination rates. Secondly, negative stopping angles can be observed for thick layers under high rates of inclination. Under such conditions, granular flows have high inertia allowing them to sustain positive velocities despite the inclination angle already turning negative. Thirdly, the results for the various rates seem to collapse onto one solution for very small thicknesses $h \lesssim 20d$. Lastly, by reducing the rate of inclination, the continuum solution approaches the quasi-static solution in (7).

In combining these results and focusing on the continuum model, another important observation can be made: The resulting starting angle θ_{start} is always greater than the 'true' critical angle $\tan^{-1}\mu_s$. This directly follows from the quasi-static solution (6) for $u_t > 0$. The observation is illustrated in Figure 4, where the results have been plotted for various values of u_t while keeping the inclination rate constant at $1\,°/s$. These results demonstrate that θ_{start} is greater than $\tan^{-1}\mu_s = 15.3°$ (dashed line) for any thickness and that θ_{start} increases with u_t. Similarly, $\theta_{stop} \leq \tan^{-1}\mu_s$, assuming $u_t = 0$ in the case of the stopping simulation. As a consequence, a hysteresis-like behaviour is obtained with $\theta_{start} > \theta_{stop}$ despite no hysteresis being included in the underlying constitutive law. This apparent hysteresis is solely due to the inertia of the flow. Furthermore, this deviation between θ_{start} and θ_{stop} increases with increasing rate of inclination or increasing threshold velocity.

When comparing the DEM and the continuum results, there is a good agreement between the solutions for granular flows for thicknesses $h \gtrsim 25d$ for the stopping simulations and $h \gtrsim 50d$ for the starting simulations. On the other hand, a larger discrepancy between the two solutions can be observed for the shallower flows. In particular, DEM simulations provide systematically higher θ_{start} and θ_{stop} for small thicknesses. This effect is unrelated

to inertia, as it remains present for vanishing u_t and $\dot{\theta}$. Instead, it may be attributed to non-local rheology [20, 21], manifested by a finite correlation length, which is not included in the continuum model. Such a length scale could span the entire layer for small enough h. As a result, shallower layers are stronger and start/cease flowing at a greater $\theta_{start}/\theta_{stop}$. In addition, DEM simulations exhibit a significant variability in θ_{start} depending on the initial configuration of grains. Tiny differences in porosity or structure of interlocking grains within the initial packing were observed to lead up to 2° difference in θ_{start} for otherwise the same conditions and protocol parameters. We therefore repeated the entire protocol for 4 different initial configurations and present in Figure 3 the averaged values together with error bars calculated as the standard deviations. This configurational variability is much lower in the case of stopping simulations, where the error bars are generally smaller than the marker size. It is also noted that the configurational variability is larger than finite size effects associated with using finite periodic cell width in the DEM simulations.

The inertial effects studied here are manifested by departure of the measured flow velocity (Figure 2) and $\theta_{start/stop}$ (Figure 3) from the quasi-static solutions given by Eqs. (6) and (7), in which inertia of the flow is neglected. To assess conditions under which the inertial effects arise, two competing time scales need to be considered. The first time scale is associated with acceleration or deceleration of the flow upon change in the inclination angle. If the inclination changes by $d\theta$, the flow velocity tends to approach the steady-state velocity at the new inclination angle. The time scale, t_1, associated with the acceleration of the flow is [8] $t_1 = |du_{ss}|/g = |u_{ss}(\theta + d\theta) - u_{ss}(\theta)|/g$, where u_{ss} is the quasistatic velocity given by Eq. (6) for $z = h$. The second time scale, $t_2 = |d\theta|/\dot{\theta}$, is associated with rotation of the chute, being the time to change the inclination angle by $d\theta$. The inertial effects arise if the time scale for the change in the inclination angle is shorter than the time scale for the flow velocity to adjust to the change in the inclination angle. Imposing $t_1 > t_2$ gives

$$|\dot{\theta}| > \frac{g}{du_{ss}/d\theta} \simeq \frac{\beta d}{h^{3/2}} \sqrt{\frac{g}{\phi}} \frac{\sqrt{\cos\theta}}{\left[\frac{1}{\cos\theta} - \frac{1}{2}(\tan\theta - \mu_s)\sin\theta\right]} \,, \tag{8}$$

where algebraic factors of order one have been omitted. The last factor is a slowly varying function of θ, attaining values 0.88-0.95 in the range of $\theta = 15.3 - 27°$, corresponding with the range of θ_{start} depicted in Figure 3a, and can be substituted with unity within the same accuracy. Hence, if the rate of inclination $|\dot{\theta}|$ is greater than a threshold $\frac{\beta d}{h^{3/2}}\sqrt{\frac{g}{\phi}}$, then
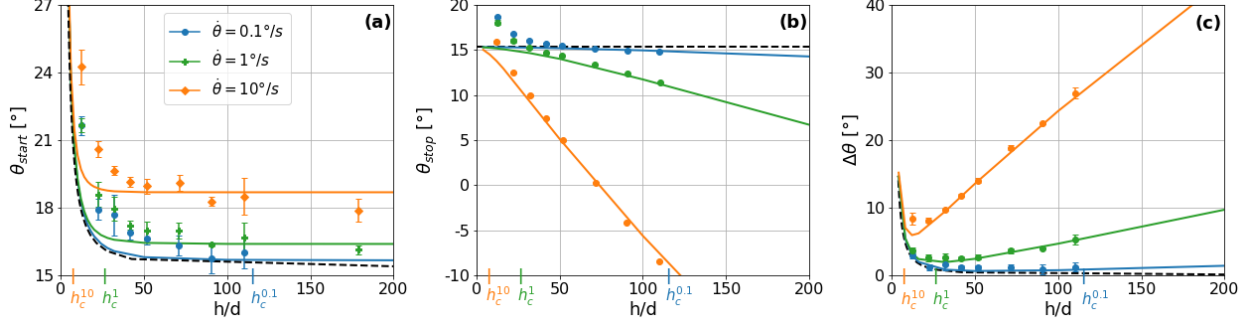
14

FIG. 3. The results of the DEM solution (markers, with error bars representing one standard deviation), continuum solution (solid lines) and quasi-static solution (dashed line) for a) starting ($u_t = 0.1$ m/s); b) stopping ($u_t = 0$ m/s) simulations; and c) the corresponding apparent hysteresis $\Delta\theta = \theta_{start} - \theta_{stop}$. The critical thicknesses h_c based on (9) are indicated on the x-axis for the three rates of inclination.

inertial effects should be considered, as the measured angle of repose will depend on $\dot\theta$.

This criterion can be inverted to define a critical thickness

$$h_c^{3/2} = \frac{\beta d}{|\dot\theta|}\sqrt{\frac{g}{\phi}}. \tag{9}$$

For thin flows, $h < h_c$, inertial effects can be neglected, whereas for thicker flows, $h > h_c$, inertial effects become important, and measurements of θ_{start} and θ_{stop} will suffer from spurious dependency on $\dot\theta$. Predicted values of h_c for three different rates of inclination are indicated in Figure 3. This prediction explains why results of the continuum model closely match the quasi-static solution up to a certain flow thickness, which increases with decreasing $|\dot\theta|$. Note however that even for as slow a rate as $0.1°/s$, the model data deviate from the quasi-static limit for $h > 100d$. Since macroscopic granular flows are often more than hundreds of grains thick, the inertial effects should be considered in situations when the inclination varies.

III. INCLINED CHUTE WITH EROSION: EXPERIMENTS

To additionally demonstrate the the role of inertia in a real and non-idealised inclining chute set-up, a series of experiments have been conducted in an attempt to replicate and then extend the study by [10]. In the previous work, the authors examined the starting and stopping mechanisms by performing inclined chute experiments, measuring the angle
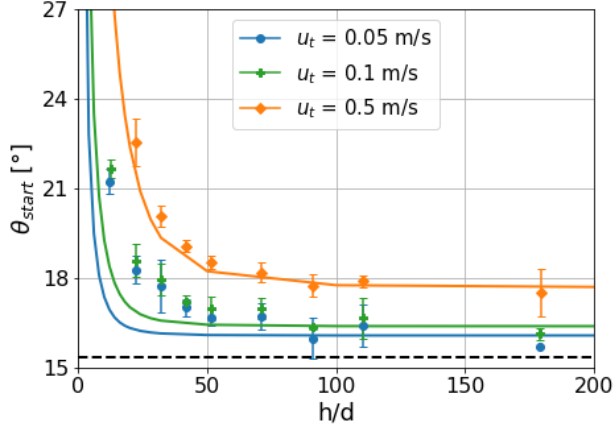
FIG. 4. The results of the DEM solution (markers, with error bars representing one standard deviation), continuum solution (solid lines) and quasi-static solution for $u_t = 0$ (dashed line) showing the effect of u_t for fixed $\dot{\theta} = 1$ °/s.

at which the grains start to flow (θ_{start}) and the corresponding thickness of the residual deposit layer (h_{stop}) at that same angle, after material has partially eroded from the bed. This experimental procedure is therefore different from the previously described numerical protocol of the stopping simulations, as the material is allowed to flow out of the chute and come to a rest, while the inclination angle remains constant. While staying true to the procedure described in [10], this new experimental series studies the flow of granular material down an inclined chute while mapping the influence of the controlling rate of inclination $\dot{\theta}$ and threshold velocity u_t parameters.

A.   Setup and Protocol

A schematic representation of the setup is shown on Figure 5a. The experimental protocol is as follows: the chute, initially inclined at a 14.3° angle, is first carefully filled up with glass beads (with a mean diameter d of 0.75 mm) to form a uniform layer with initial thickness h_{start}. While recording the material with a camera from above at a rate of 60 frames per second, the inclination angle of the chute θ is increased by lifting the chute at a prescribed rate r using a vertical translation stage. This continues as grains start to flow until motion is observed over the full length of the camera frame, meaning that a flow has already developed. At this instant of $\theta = \theta_{start}$, the inclination of the chute is manually stopped and a light

16

simultaneously switched on to aid image post-processing. The flow partially erodes into the initial layer and the granular material then flows out of the open chute, leaving behind a deposit layer of thickness $h_{stop} < h_{start}$. The process is then repeated by further increasing the inclination angle to initiate flow again. Several runs have been performed for different layer thicknesses and two different rates of the vertical translation stage: a slow rate (r = 1 mm/s) and a fast rate (r = 10 mm/s). These correspond to an initial rate of inclination $\dot{\theta}$ of $0.1°/s$ and $1°/s$, respectively, which, for future analysis purposes, have been assumed to remain constant throughout the course of the experiment.

Once the material has come to a rest, an image is taken from the side of the chute at a location corresponding to the centre of the top camera view. The layer thickness is inferred from these images during post-processing of the data, and the angle at each time point $\theta(t)$ is calculated from the position of the vertical inclination stage with approximately a $0.1°$ precision. The threshold velocity u_t is found through the post-processing of the top camera images by means of Particle Image Velocimetry (PIV) analysis in PIVLab for MATLAB [22]. Figure 5b shows a stack of some example frames that are used in the post-processing of the data. The moment at which the light is switched on can be detected in the video frames, and thus allows for the evaluation of u_t at that exact instant through PIV analysis. The mean u_t is taken over all of the patches in the whole region of interest, which may consist of both flowing and stationary patches.

Figure 5c depicts an exemplary spatio-temporal plot of the top camera images, formed by taking the central line of pixels in the x-direction from each subsequent image. The plot can be subdivided into three main parts: an initially static period $(t_0 < t < t_1)$, followed by a period of flow where the movement of the particles start at the bottom of the chute and travels upwards until a full avalanche over the whole length has occurred $(t = t_t)$. The flow subsequently comes to a rest resulting in a final static state $(t_t < t < t_{end})$. The time t_t is the moment at which the velocity reaches a threshold value u_t. This, inevitably, is related to the observer, who determines when an avalanche has occurred and therefore arrests the raising of the chute. The velocity threshold is thus not known prior to the experiment, but can be computed from PIV analysis of the camera images
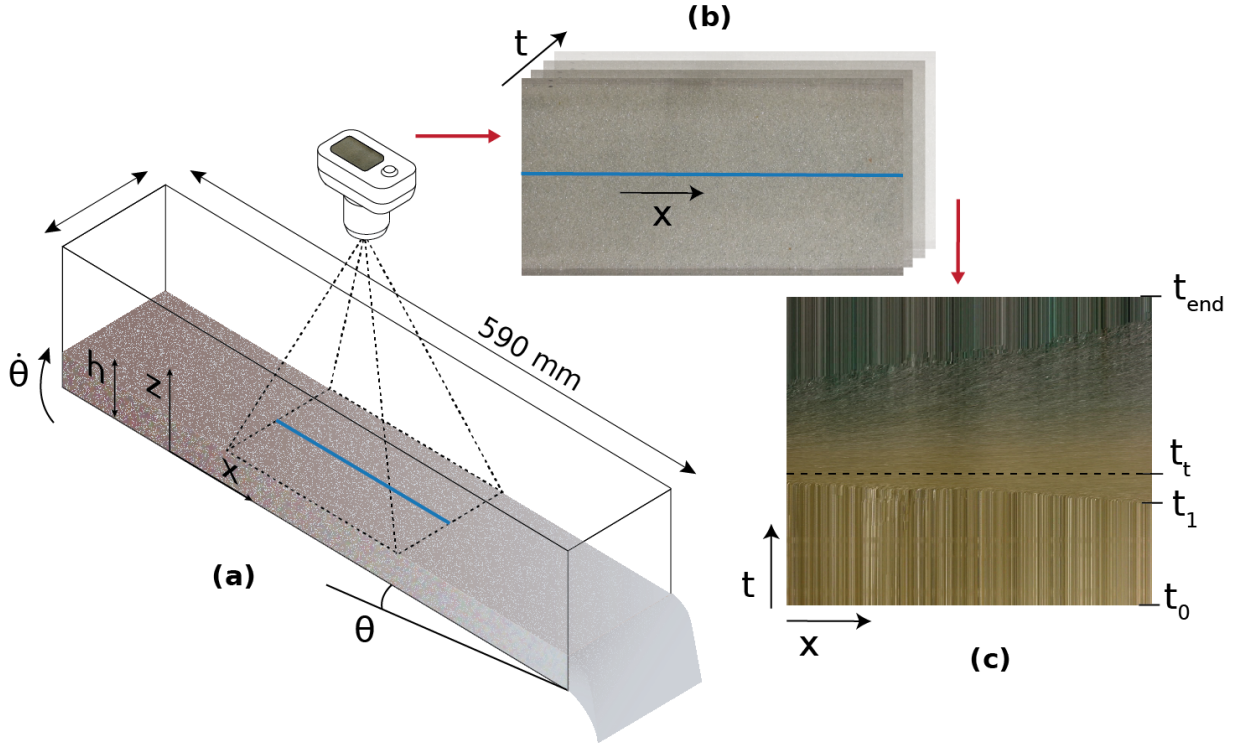
.

FIG. 5. Experimental set-up and protocol: *a*) Schematic of the set-up, indicating the chute, inclination angle θ, rate of inclination $\dot{\theta}$ and position of the top camera. *b*) Successive camera frames, showing the line of pixels used for constructing spatio-temporal plots. *c*) An example spatio-temporal plot identifying stationary ($t_0 < t < t_1$), acceleration ($t_1 < t < t_t$), and deceleration ($t_t < t < t_{end}$) phases. The dashed line indicates the time t_t at which the velocity reaches u_t.

B. Effect of Protocol Parameters

Figure 6 depicts an overview of the experimental results. Figure 6a shows the θ_{start} and h_{stop} measurements for the slow and fast rates. The θ_{start} and h_{stop} measurements come in pairs, each pair originating from one continuous experimental run. Indicative interpolation curves have been included emphasising the general trend of the data. The experimental results show a noticeable difference between the $0.1°/s$ and $1°/s$ inclination rate, highlighting that the fast rate of inclination generally leads to a value of θ_{start} that is approximately $2°$ higher than for the slow rate, given the same initial thickness. Human reaction time may be partially responsible for this difference since, for the same reaction time, experiments at the faster inclination rate will reach a higher angle before the slope is arrested. However, using

18

the imposed rates and a visual human reaction time of approximately 0.25 s [23], a simple calculation shows that this reaction alone cannot explain the significant difference in θ_{start} between the two rates. However, greater inertia, as a result of the faster rate, does offer a plausible explanation. For the h_{stop} measurements, the trend lines appear to collapse into one and little to no difference between the rates can be distinguished. This is in line with expectations since there is no inclination angle variation during the stopping phase of the experiment, as prescribed by the experimental protocol.

Figure 6b examines the effect of the threshold velocity u_t on the starting and stopping thicknesses. We can see an increase in both of these quantities with increasing values of u_t. However, a more interesting measure is the difference between the starting and stopping thicknesses, $\Delta h = h_{start} - h_{stop}$, which can be interpreted as the amount of erosion of material. Figures 6c and 6d examine the relation between this erosion measure and the starting thickness h_{start} and mean threshold u_t. In contrast to the relatively small effect of the rate of inclination on h_{stop}, the amount of erosion, and thus h_{stop} itself, does depend strongly on both u_t and h_{start}, showing a positive correlation between Δh and h_{start} (Figure 6c), and Δh and u_t (Figure 6d). Once again, both of these parameters are directly related to the overall momentum in the system, with thicker, faster flows having greater inertia.

IV. DISCUSSION AND CONCLUSION

In attempts to improve the $\mu(I)$-rheology, the current line of research of granular media near the flow to no-flow transition focuses on apparent constitutive mechanisms occurring at the particle scale. This has led to sophisticated, but often complex, relations based on different physical explanations at the microscopic scale. For example, different authors have suggested growing cluster formations [24], self-activated processes of stress fluctuations [25, 26], or an increasing number of sliding contacts [27] leading to mechanical noise [28]. Following a different approach, this study takes a step back and highlights the importance of the role of inertia at the bulk scale (as per classical definition in physics) in the description of shallow granular flows, which appears to have been partially overlooked in previous studies. On the other hand, inertia effects at the particle scale have been related to the Stokes number and interparticle friction in the field of immersed granular media [29, 30]. In this study, the prominence of the inertia is illustrated in a threefold manner: through a two-dimensional
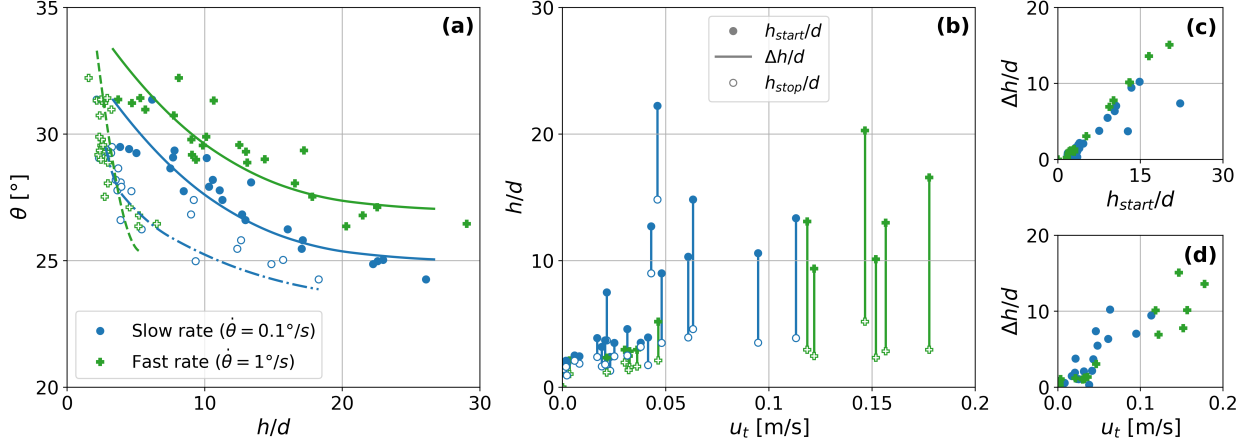
FIG. 6. The experimental results demonstrating the effects of the protocol parameters. a) Measurements of the starting angle θ_{start} (solid markers) and the thickness of the deposit when the flow stops h_{stop} (open markers), for the different rates of inclination. b) The starting (h_{start}) and stopping (h_{stop}) thicknesses of the granular layer against the threshold velocity u_t. The length of the bars gives measure of erosion $\Delta h = h_{start} - h_{stop}$. The effect of the initial thickness h_{start} and threshold velocity u_t on Δh are shown on plots c) and d), respectively.

DEM study as well as a corresponding one-dimensional depth-resolved model, both without surface erosion, and finally in an experimental study with surface erosion.

The experimental approach is a reflection of similar experiments performed previously. It is simple, yet effective in strengthening the argument, as it exemplifies and confirms the significance of the two protocol parameters $\dot{\theta}$ and u_t on the results. The experimental results demonstrate that a) $\theta_{start} > \theta_{stop}$ for the same flow thickness, b) both θ_{start} and θ_{stop} depend on the flow thickness h, c) θ_{start} increases with increasing the magnitude of the inclination rate. The same does not apply to θ_{stop}, which is independent of the rate of inclination. This can be attributed to the experimental protocol in which the inclination angle is fixed as the flow comes to a rest. In conserving the simplicity of the protocol, the reproducibility of the experiment is increased.

Furthermore, in order to be able to properly study the inertia effects on the boundary value problem in a controlled setup, a DEM study has been performed and the results of this study are compared with a continuum solution. These simulation results show that a) the starting angle is greater than the stopping angle, $\theta_{start} > \theta_{stop}$, and b) both θ_{start} and θ_{stop} depend on the flow thickness h, despite no hysteresis or intrinsic material length scales

being included in the constitutive law. The adopted model only solves for the fundamental momentum equation in the x-direction, and, apart from the standard $\mu(I)$-rheology, requires no additional constitutive assumptions. The results demonstrate that this hysteresis-like behaviour is a direct consequence of the inertia effects governed by the protocol parameters: The non-zero threshold velocity is the root cause of the starting angle being greater than the 'true' critical angle, $\theta_{start} > \tan^{-1} \mu_s$. For the stopping simulations, where the initial system already exhibits inertia, rate effects exist despite $u_t = 0$. As a consequence, the stopping angle will be smaller than the 'true' critical angle, $\theta_{stop} < \tan^{-1} \mu_s$. In both cases, higher inclination rates increase the deviation from the true critical angle. The order of magnitude of this observed apparent hysteresis ranges from a few degrees to tens of degrees depending on the employed rate of inclination and layer thickness.

Moreover, out of the two protocol parameters, the determination of the velocity threshold is more ambiguous. However, we highlight that this parameter is an inevitable part of similar experimental studies and should be appropriately accounted for when interpreting results. Contrary to the inclination rate, which can be minimised to reduce inertial effects, the velocity threshold depends on the experimental observer and the granular system under consideration. For that reason, no universal value for u_t is advocated here.

By considering the transient time needed to reach a new steady-state velocity upon changing θ, we derive a critical rate of inclination and corresponding critical layer thickness, above which inertia effects govern the solution. In agreement with experimental results (Figures 5a and c), for larger flow thicknesses, the inertia effect dominates the problem. This is a relevant finding in terms of practical applications that go beyond laboratory settings such as field-scale landslides and avalanches, where the thickness of the granular flow may easily be more than thousands of grain diameters. Another important observation is the possibility of negative stopping angles for thick flows under larger (in absolute terms) rates of inclination. This phenomenon, described by both the DEM and the continuum solutions, matches real-life avalanches and debris flows whose run-out progresses along horizontal planes (zero angle) and even uphill (negative inclination), provided that they have enough inertia.

At the same time, it is acknowledged that an extension of the current rheological law, by including for example non-local effects [20, 31–33], is required to fully represent all observations. In particular, with regards to the description of very thin granular layers, for which the results imply that not only inertia is at play. Exemplary results can be found in

the work by Mowlavi & Kamrin (2021) [21] who carefully minimised the inertia effects in their study on the interplay between hysteresis and nonlocality. Here, it is thus accordingly stressed that before developing new constitutive concepts, the contribution of inertia as part of the boundary value problem needs to be isolated and properly understood. Similarly, it has been demonstrated that, in porous media, macroscopic velocity weakening should not be taken as a necessary condition for explaining stick-slip dynamics [34], which serves as a related example about the necessity of complicated constitutive laws in other materials.

ACKNOWLEDGMENTS

Appendix A: Discrete Element Simulation Details

The discrete element method solves dynamics of individual grains, considered as spherical particles, by time integration of momentum conservation laws for the translational and rotational degrees of freedom

$$m_i \frac{\mathrm{d}\mathbf{u}_i}{\mathrm{d}t} = \sum_j \mathbf{F}_{ij} + m_i \mathbf{g}\,, \tag{A1}$$

$$I_i \frac{\mathrm{d}\boldsymbol{\omega}_i}{\mathrm{d}t} = \frac{d_i}{2} \sum_j \mathbf{n}_{ij} \times \mathbf{F}_{ij}\,, \tag{A2}$$

where $\mathbf{u}_i$, $\boldsymbol{\omega}_i$, m_i, d_i, and $I_i = m_i d_i^2/10$ are velocity, angular velocity, mass, diameter, and moment of inertia of grain i, respectively, and $\mathbf{g}$ is the gravitational acceleration. The right-hand sides of (A1) and (A2) are the total force and torque acting on grain i. The total force consists of pair-wise forces $\mathbf{F}_{ij}$ exerted by all grains j contacting i. A unit normal vector to the contact between grains i and j, is defined as $\mathbf{n}_{ij} = \mathbf{r}_{ij}/r_{ij}$, where $\mathbf{r}_{ij} = \mathbf{r}_j - \mathbf{r}_i$ is the vector connecting centres of grains i and j (and r_{ij} is its magnitude).

The contact force between grains i and j, $\mathbf{F}_{ij}$, is controlled by the overlap of the two "soft" spheres: $\delta_{ij} \equiv d_i/2 + d_j/2 - r_{ij}$. The two grains interact only if they overlap, $\delta_{ij} > 0$. In that case, the normal (n) and the tangential (t) components of $\mathbf{F}_{ij} = \mathbf{F}_{ij}^n + \mathbf{F}_{ij}^t$ are given by

$$\mathbf{F}_{ij}^n = -k_n \delta_{ij} \mathbf{n}_{ij} + \gamma_n m_{\text{eff}} \mathbf{u}_{ij}^n \,, \tag{A3}$$

$$\mathbf{F}_{ij}^t = k_t \mathbf{t}_{ij} + \gamma_t m_{\text{eff}} \mathbf{u}_{ij}^t \,, \qquad \text{if} \quad F_{ij}^t < \mu_g F_{ij}^n \,, \tag{A4}$$

$$\mathbf{F}_{ij}^t = \mu_g F_{ij}^n \frac{\mathbf{t}_{ij}}{t_{ij}} \,, \qquad\qquad \text{otherwise}\,.$$

The first terms in (A3)-(A4) are elastic forces, represented by springs of stiffnesses k_n and k_t, which are proportional to the overlaps in the normal and the tangential directions. The later is calculated by integrating the following equation since the time the contact has been created

$$\frac{\mathrm{d}\mathbf{t}_{ij}}{\mathrm{d}t} = \mathbf{u}_{ij}^t - \frac{\mathbf{t}_{ij} \cdot (\mathbf{u}_j - \mathbf{u}_i)}{r_{ij}^2} \mathbf{r}_{ij} \,, \tag{A5}$$

where the last term comes from rigid body rotation around the contact point and insures that $\mathbf{t}_{ij}$ always lies in the tangent plane; $\mathbf{u}_{ij}^t = \mathbf{u}_j - \mathbf{u}_i - \mathbf{u}_{ij}^n + 0.5(d_i \boldsymbol{\omega}_i + d_j \boldsymbol{\omega}_j) \times \mathbf{r}_{ij}/r_{ij}$ is the relative velocity between the grains projected into the tangent plane; while $\mathbf{u}_{ij}^n = (\mathbf{u}_j - \mathbf{u}_i) \cdot \mathbf{n}_{ij}\, \mathbf{n}_{ij}$ is the normal component of the relative velocity.

The second terms in (A3)-(A4) are damping forces, which make collisions inelastic. These forces are proportional to the damping coefficient γ_n or γ_t, the effective mass of grains i and j, $m_{\text{eff}} = m_i m_j/(m_i + m_j)$, and to the relative velocity projected into the normal or the tangential direction.

The tangential component of the inter-particle force (A4) is truncated by the Coulomb friction force: $\mu^* F_{ij}^n$, where μ^* is grain surface friction coefficient. Contacts subject to a greater applied tangential force than this limit slide, and the difference between the applied and the friction force is transformed into grains' inertia.

The equations of motion, (A1) and (A2), are integrated in a series of discrete time instants using the velocity Verlet integrator [12] with a time step $\Delta t = 0.1\, t_{\text{col}}$, where $t_{\text{col}} = d\sqrt{\rho/E}$ is the time scale for a collision of two grains with diameter d, mass density ρ and Young's modulus, E. This choice insures that the fastest momentum transfer, i.e. propagation of elastic waves, is well resolved.

The distribution of grain sizes is derived from Gaussian distribution with the mean size and the standard deviation both equal to $1d$ and is truncated to achieve polydispersity of

±20%.

---

[1] C. H. Scholz, Earthquakes and friction laws, Nature **391**, 37 (1998).

[2] A. Lucas, A. Mangeney, and J. P. Ampuero, Frictional velocity-weakening in landslides on earth and on other planetary bodies, Nature communications **5**, 3417 (2014).

[3] GDR MiDi, On dense granular flows, The European Physical Journal E **14**, 10.1140/epje/i2003-10153-0 (2004).

[4] P. Jop, Y. Forterre, and O. Pouliquen, Crucial role of sidewalls in granular surface flows: consequences for the rheology, Journal of Fluid Mechanics **541**, 10.1017/S0022112005005987 (2005).

[5] P. Jop, Y. Forterre, and O. Pouliquen, A constitutive law for dense granular flows, Nature **441**, 10.1038/nature04801 (2006).

[6] O. Coquand, M. Sperl, and W. Kranz, Integration through transients approach to the μ (i) rheology, Physical Review E **102**, 032602 (2020).

[7] L. Staron, P. Y. Lagree, and S. Popinet, The granular silo as a continuum plastic flow: The hour-glass vs the clepsydra, Phys. Fluids **24**, 103301 (2012).

[8] S. Parez, E. Aharonov, and R. Toussaint, Unsteady granular flows down an inclined plane, Physical Review E **93**, 10.1103/PhysRevE.93.042902 (2016).

[9] T. T. Vo, S. Nezamabadi, P. Mutabaruka, J.-Y. Delenne, and F. Radjai, Additive rheology of complex granular flows, Nature communications **11**, 1 (2020).

[10] O. Pouliqen and Y. Forterre, Friction law for dense granular flows: application to the motion of a mass down a rough inclined plane, Journal of Fluid Mechanics **453**, 10.1017/S0022112001006796 (2002).

[11] O. Pouliquen, Scaling laws in granular flows down rough inclined planes, Physics of Fluids **11**, 10.1063/1.869928 (1999).

[12] P. A. Cundall and O. D. Strack, A discrete numerical model for granular assemblies, Géotechnique **29**, 47 (1979).

[13] S. Parez, T. Travnickova, M. Svoboda, and E. Aharonov, Strain localization in planar shear of granular media: the role of porosity and boundary conditions, The European Physical Journal E **44**, 134 (2021).

[14] S. Parez, M. Kozakovic, and J. Havlica, Pore pressure drop during dynamic rupture and conditions for dilatancy hardening, Journal of Geophysical Research: Solid Earth **128**, e2023JB026396 (2023), e2023JB026396 2023JB026396, https://agupubs.onlinelibrary.wiley.com/doi/pdf/10.1029/2023JB026396.

[15] F. da Cruz, S. Emam, M. Prochnow, J.-N. Roux, and F. Chevoir, Rheophysics of dense granular materials: Discrete simulation of plane shear flows, Phys. Rev. E **72**, 021309 (2005).

[16] L. E. Silbert, D. Ertas, G. S. Grest, T. C. Halsey, D. Levine, and S. J. Plimpton, Granular flow down an inclined plane: Bagnold scaling and rheology, Phys. Rev. E **64**, 051302 (2001).

[17] S. Parez and E. Aharonov, Long runout landslides: a solution from granular mechanics, Frontiers in Physics **3**, 80 (2015).

[18] J. Gray and A. Edwards, A depth-averaged rheology for shallow granular free-surface flows, Journal of Fluid Mechanics **755**, jfm.2014.450 (2014).

[19] A. Edwards and J. Gray, Erosion–deposition waves in shallow granular free-surface flows, Journal of Fluid Mechanics **762**, 10.1017/jfm.2014.643 (2015).

[20] K. Kamrin and D. L. Henann, Nonlocal modeling of granular flows down inclines, Soft Matter **11**, 10.1039/C4SM01838A (2015).

[21] S. Mowlavi and K. Kamrin, Interplay between hysteresis and nonlocality during onset and arrest of flow in granular materials, Soft Matter **17**, 7359 (2021).

[22] W. Thielicke and R. Sonntag, Particle image velocimetry for matlab: Accuracy and enhanced algorithms in pivlab., Journal of Open Research Software **9** (2021).

[23] A. Jain, R. Bansal, A. Kumar, and K. Singh, A comparative study of visual and auditory reaction times on the basis of gender and physical activity levels of medical first year students, International Journal of Applied and Basic Medical Research **5**, 124 (2015).

[24] P. Mills, P. Rognon, and F. Chevoir, Rheology and structure of granular materials near the jamming transition, EPL (Europhysics Letters) **81**, 64005 (2008).

[25] O. Pouliquen, Y. Forterre, and S. Le Dizes, Slow dense granular flows as a self-induced process, Advances in Complex Systems **04**, 10.1142/S0219525901000358 (2001).

[26] O. Pouliquen and Y. Forterre, A non-local rheology for dense granular flows, Philosophical Transactions of the Royal Society A: Mathematical, Physical and Engineering Sciences **367**, 5091 (2009).

[27] M. Wyart, On the dependence of the avalanche angle on the granular layer thickness, EPL

(Europhysics Letters) **85**, 10.1209/0295-5075/85/24003 (2009).

[28] E. DeGiuli and M. Wyart, Friction law and hysteresis in granular materials, Proceedings of the National Academy of Sciences **114**, 10.1073/pnas.1706105114 (2017).

[29] S. Courrech du Pont, P. Gondret, B. Perrin, and M. Rabaud, Granular avalanches in fluids, Physical review letters **90**, 044301 (2003).

[30] H. Perrin, C. Clavaud, M. Wyart, B. Metzger, and Y. Forterre, Interparticle friction leads to nonmonotonic flow curves and hysteresis in viscous suspensions, Physical Review X **9**, 031027 (2019).

[31] M. Bouzid, M. Trulsson, P. Claudin, E. Clément, and B. Andreotti, Nonlocal rheology of granular flows across yield conditions, Physical Review Letters **111**, 238301 (2013).

[32] M. Bouzid, A. Izzet, M. Trulsson, E. Clément, P. Claudin, and B. Andreotti, Non-local rheology in dense granular flows, The European Physical Journal E **38**, 125 (2015).

[33] H. Perrin, M. Wyart, B. Metzger, and Y. Forterre, Nonlocal effects reflect the jamming criticality in frictionless granular flows down inclines, Physical Review Letters **126**, 10.1103/PhysRevLett.126.228002 (2021).

[34] J. R. Valdes, F. Guillard, and I. Einav, Evidence that strain-rate softening is not necessary for material instability patterns, Physical review letters **119**, 118004 (2017).